Evolution of the Raman spectra from single-, few-, and many-layer graphene with increasing disorder

E. H. Martins Ferreira,[1] Marcus V. O. Moutinho,[2] F. Stavale,[1] M. M. Lucchese,[1,3] Rodrigo B. Capaz,[1,2] C. A. Achete,[1,4] and A. Jorio[1,5]

[1]*Divisão de Metrologia de Materiais, Instituto Nacional de Metrologia, Normalização e Qualidade Industrial (INMETRO), Duque de Caxias 25250-020, RJ, Brazil*

[2]*Instituto de Física, Universidade Federal do Rio de Janeiro, Cx. Postal 68528, Rio de Janeiro 21941-972, RJ, Brazil*

[3]*Centro de Ciências Exatas e Tecnológicas, Universidade Federal do Pampa, Bagé, Rio Grande do Sul, Brazil*

[4]*Programa de Engenharia Metalúrgica e de Materiais (PEMM), Universidade Federal do Rio de Janeiro, Cx. Postal 68505, Rio de Janeiro 21945-970, RJ, Brazil*

[5]*Depto. de Física, Universidade Federal de Minas Gerais, Belo Horizonte 30123-970, MG, Brazil*

(Received 3 May 2010; published 15 September 2010)

We report on the micro-Raman spectroscopy of monolayer, bilayer, trilayer, and many layers of graphene (graphite) bombarded by low-energy argon ions with different doses. The evolution of peak frequencies, intensities, linewidths, and areas of the main Raman bands of graphene is analyzed as function of the distance between defects and number of layers. We describe the disorder-induced frequency shifts and the increase in the linewidth of the Raman bands by means of a spatial-correlation model. Also, the evolution of the relative areas A_D/A_G, $A_{D'}/A_G$, and $A_{G'}/A_G$ is described by a phenomenological model. The present results can be used to fully characterize disorder in graphene systems.

DOI: 10.1103/PhysRevB.82.125429 PACS number(s): 61.48.Gh, 78.67.Wj, 78.30.Ly, 61.72.Dd

I. INTRODUCTION

Graphene is a planar sheet of sp^2-bonded carbon atoms arranged on a hexagonal lattice with two-dimensional (2D) exceptional electronic transport.[1–4] It is a two-dimensional semimetal where the overlap between the valence and the conduction bands occurs in two single points at the border of the Brillouin zone, named K and K′. The reported carrier mobilities are as high as 200 000 $cm^2/V\,s$.[5] Graphene exhibits also high thermal conductivity (~3080 W/mK) (Ref. 6) and high chemical and mechanical stability, which makes it promising material for future nanoelectronic devices.[7] These interesting properties extend for single and few layers of graphene,[8–10] thus making graphene physics even richer and attractive.

It is well known that disorder plays an important role in graphene properties.[11–13] The micro-Raman spectroscopy is a nondestructive, rapid, and likely the most sensitive technique for studying disorder in nanostructured sp^2 carbon systems with the occurrence of defect-induced peaks.[14–21] The presence of disorder in sp^2 hybridized carbon systems, from the three-dimensional graphite to the one-dimensional carbon nanotubes, leads to rich and intriguing phenomena that have been extensively studied by resonance Raman spectroscopy.[15–21]

Defects break the momentum conservation requirement $q=0$ for the first-order Raman allowed phonons but, intriguingly, standard descriptions of disorder effects in the Raman spectrum involve phonons precisely fulfilling resonance conditions selected by momentum conservation.[17,18] This contradictory explanation of local disorder effects using crystal **k**-space selection rules represents the initial motivation for this study. In the Raman-scattering process, a photon generates an electron-hole pair and the excited electron is further scattered by phonons. Due to momentum conservation requirements in periodic systems, the first-order Raman-scattering process generates only Γ point phonons (wave vector $q=0$) where the electrons are scattered by phonons with energy exchange but no wave-vector variation. This process, labeled G (from graphite), is observed in the Raman spectrum of any number of layers graphene at ~1580 cm^{-1} and is related to the in-plane stretching of the C-C bonds.[14,15] When the periodic lattice of graphene is broken by defects, the momentum conservation requirement is also broken and all phonons in the Brillouin zone become Raman allowed, which could result on a phonon-density-of-states-like Raman spectrum. However, resonant electron-phonon scattering processes connecting real electronic states are privileged[17,18] and energy conservation requirements impose that the Raman spectrum of disordered graphene exhibits two new sharp features at approximately 1350 cm^{-1} (D band) and 1620 cm^{-1} (D′ band). These intervalley (D) and intravalley (D′) defect-induced resonant scattering processes are the ones mainly responsible for electron decoherence in optics and transport phenomena in sp^2 carbons.[22–24] Those bands are also dispersive and hence their actual positions depend on the laser excitation energy.[25,26] Raman spectroscopy has been used recently to investigate and quantify low-energy ion-induced defects in graphite[27] and single layer graphene.[28]

In this work, we report the evolution of defect-induced Raman features in graphene systems submitted to different doses of argon-ion sputtering in monolayer (M), bilayer (B), trilayer (T), and ~50 layers of graphene (graphite). We use a spatial-correlation model to describe the shift in the frequency and the change in the linewidth of the main Raman peaks (D, G, D′, and G′) of a monolayer graphene caused by the presence of disorder in the system. We also extend the phenomenological model proposed in Ref. 28 to describe the evolution of the relative peak areas A_D/A_G, $A_{D'}/A_G$, and $A_{G'}/A_G$.

This paper is organized as follows: in Sec. II, we describe the experimental details of our work; Sec. III fully describe the experimental results, including the defect-induced evolution of frequency, width, and intensity for the main Raman features (D, G, D′, and G′ bands), as well as the evolution of overtones and combination modes; Sections IV and V present our models to describe the experimental results displayed in Sec. III. While the frequency and linewidth evolutions are described within the same methodology, which we call the spatial correlation model, the intensities are described using the phenomenological model we introduced earlier in Ref. 28; Sec. VI reports how these values change by changing the number of layers, although the discussion there is more qualitative. Finally, Sec. VII summarizes the work.

II. EXPERIMENTAL DETAILS

The graphene samples were prepared by mechanical microcleavage of highly oriented pyrolytic graphite (HOPG ZYB grade, $20\times20\times2$ nm^3, NT-MDT Co.) and have been deposited on two different silicon substrates with the standard 300 nm thickness of SiO_2 on top.[2] On one substrate (S1) we have measured and identified regions with different numbers of graphene layers: monolayer, bilayer, trilayer, and many layers (~50). The identification of the few layer graphenes was done by their G′ band spectral shape[26,29] and the 50-layer graphene, that from now on we call simply by HOPG, by its atomic force microscopy (AFM) height, $h\sim15$ nm. All the graphene species were found near each other so that they were subjected to the same experimental conditions. On the other substrate (S2) we have measured and identified only two monolayer graphenes.

The ion bombardment experiments (with partial argon pressure lower than 2×10^{-5} mbar) were carried out in an OMICRON variable temperature (VT)-scanning tunnel microscope (STM) ultrahigh-vacuum system (base pressure 5×10^{-11} mbar). The ion beam ($E=90$ eV) incidence angle was 45° with respect to the normal direction of the sample's surface. Sample S1 was subjected to five different ion doses, namely, 10^{11}, 10^{12}, 10^{13}, 10^{14}, and 10^{15} ion/cm^2 and sample S2 was subject to 20 different Ar^+ bombardment doses between 1.5×10^{11} and 2.5×10^{14} Ar^+/cm^2.

Micro-Raman-scattering measurements were performed with a Horiba Jobin-Ivon T64000 triple monochromator equipped with a nitrogen cooled charge coupled device detector, in the backscattering configuration, using a 100× objective. The excitation laser energy was 2.41 eV (514.5 nm) and the power density of approximately 10^6 mW/mm^2 at the microscope objective. The micro-Raman spectra were acquired right after each bombardment procedure for every graphene sample.

Finally, STM measurements were performed on bulk HOPG subjected to the same 10^{11}, 10^{12}, 10^{13}, 10^{14}, and 10^{15} Ar^+/cm^2 bombardment doses in order to evaluate the ion damage. This procedure has been done to calibrate the experiment, as described in Ref. 28, such that we can estimate the typical distance between the defects L_D from the ion dose. We observe in the STM images that the defects are well distributed on the surface and we assume that the distribution is homogeneous such that we can use the relation $L_D=\sigma^{-1/2}$, where σ is the ion dose.

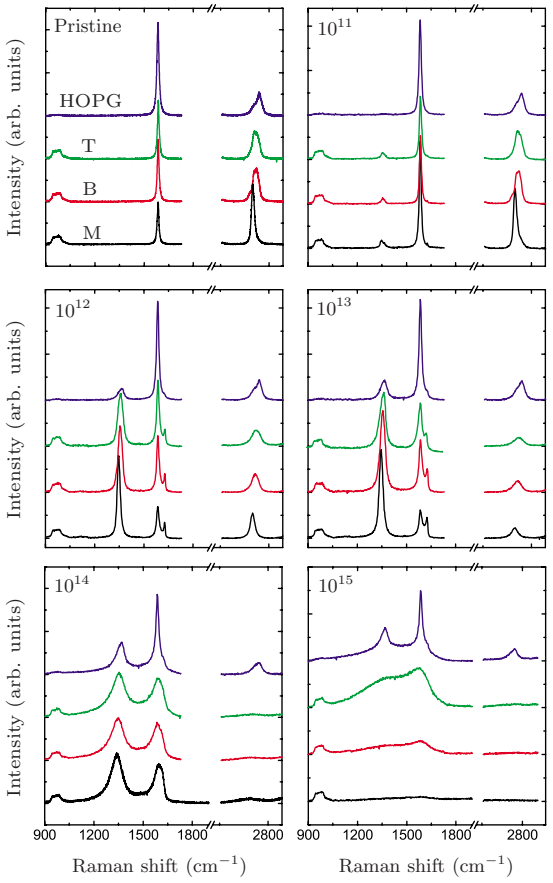

FIG. 1. (Color online) Evolution of Raman spectra for M, B, and T graphene and graphite (HOPG) samples with increasing ion dose. The ion doses are displayed in each panel in units of Ar^+/cm^2.

III. EXPERIMENTAL RESULTS

Figure 1 shows the Raman spectra of each layer in sample S1 for the different ion doses. The pristine is the Raman of the sample before any ion bombardment. The M has the G peak at 1580 cm^{-1} and the G′ peak at 2680 cm^{-1}. In the same figure we show the B spectrum. The intensity of the G peak increases while the G′ peak intensity decreases, requiring four Lorentzians for fitting.[26,30] The T spectrum is similar to the bilayer one but there are now fifteen allowed transitions.[30] However, it is not possible to resolve the 15 transitions and a satisfactory fit can be made with only six Lorentzians.[30] The graphite (HOPG) has the G peak much more intense than the G′ peak whose fitting is made with two Lorentzians (at 2690 and 2730 cm^{-1}).

After the first bombardment (10^{11} Ar^+/cm^2) we already observe the appearance of the D and D′ bands in the monolayer, bilayer, and trilayer spectra. For the 10^{12} and 10^{13} Ar^+/cm^2 doses we observe that the intensity of both D and D′ peaks increase as the G and G′ peaks broaden and decrease in intensity. The relative intensity of the D and D′

peaks with respect to the G peak is more pronounced in the monolayer, indicating that the low-energy (90 eV) ions affect only one layer. With the 10^{14} Ar^+/cm^2 dose the graphene samples start to exhibit significant peak broadening, indicating strong disorder, and this effect is more evident in the 10^{15} Ar^+/cm^2 dose. The vanishing of the peaks in the Raman spectra for monolayer graphene evidences the high dose, where 10^{15} Ar^+/cm^2 corresponds to one Ar^+ ion per four C atoms in the layer. However, the monolayer graphene has not been removed, as evidenced by further AFM analysis and heat treatment (950 °C annealing during 3 h), which partially recovered the monolayer graphene Raman signal. In graphite we still observe some order because of the large number of untouched inner layers.

In the following sections we discuss the details of the effects presented here, focusing on the evolution of the main Raman peaks of monolayer graphene in sample S2 with increasing disorder. In the graphs, there are always two types of symbols (closed and open) which correspond to two different graphenes on the same substrate and hence subjected to the same bombardment. In Sec. VI we address the multilayer case of sample S1.

A. Frequencies

Figure 2 (upper panel) shows the frequencies of several Raman peaks as they evolve with L_D for the monolayer (S2). Note that all frequencies remain approximately constant for large values of L_D, showing small shifts (on the order of few cm^{-1}) when L_D decreases below 4 nm. This shows that even at moderately large disorder regimes, the C-C bonds are still sp^2 kind, with no significant strain in the bonds. This behavior is clearly seen in the lower panel, where the shifts for each peak are shown in comparison with the theoretical model described in Sec. IV. In the inset of the upper panel, we show the frequency of the D peak (ω_D) and half the frequency of the G′ peak ($\omega_{G'}$). Although the G′ peak is often described as simply the second order of the D feature, the situation is more complex since two different scattering mechanisms are possible for the D band process (defect first and phonon second, or phonon first and defect second) while for the G′ band, only one mechanism is possible. This has been discussed for turbostratic graphite,[31] which is a good prototype of a 2D graphite, and it is here further confirmed for graphene with higher frequency accuracy. Here we find a mean difference $\Delta\omega=\omega_D-\omega_{G'}/2=4.5$ cm^{-1} which is in excellent agreement with previous results for turbostratic graphite.[31]

B. Peak widths

Figure 3 (upper panel) shows the full width at half maximum (FWHM), Γ, of all peaks as a function of L_D for the monolayer (S2). Again, for low ion doses the widths do not change considerably, showing a larger increase only for $L_D < 4$ nm. The peaks related to phonons at or near the Γ point (G and D′, respectively) have a less pronounced increase while the two peaks coming from near the K point (D and G′) show a much faster increase. In the lower panel, we show only the disorder contribution for the width ($\Delta\Gamma$),

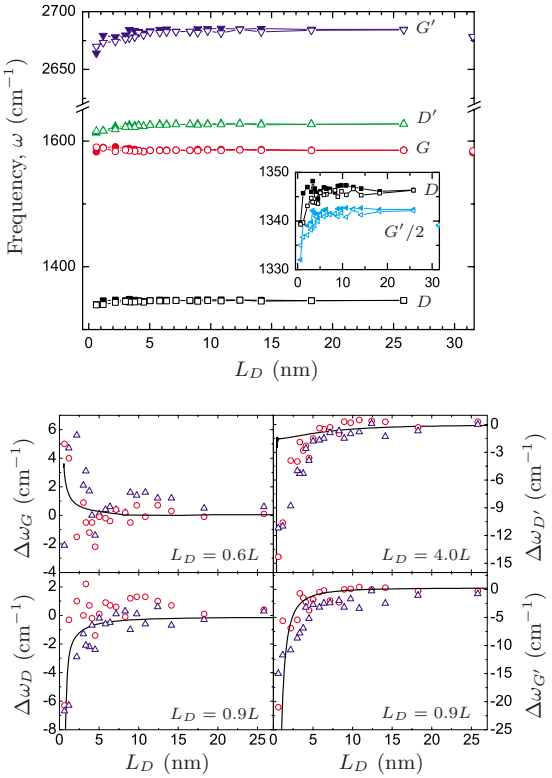

FIG. 2. (Color online) (Upper panel) Peak frequencies of the D, G, D′, and G′ bands as function of the typical distance between defects (L_D) for the monolayer (S2). The inset compares the frequency of the D band and the G′ band divided by 2, showing that we always have $\omega_{G'}/2<\omega_D$. (Lower panel) Frequency shifts with respect to the zero-disorder limit. Dots are experiments and solid lines are theoretical results based on the model described in Sec. IV. Experimental errors are ±1 cm^{-1}.

which we obtain by subtracting the zero-disorder width from the absolute width. The solid lines are the results from the model in Sec. IV, to be described below.

C. Intensities

In Fig. 4 (upper panel) we present the absolute intensities of all peaks as a function of L_D for the monolayer (S2). As the absolute Raman signal intensity depends on many measurements factors, such as laser power density, beam focus on the sample, etc., we have normalized our results by the integrated area of the G peak (A_G), which is expected to be proportional to the number of C-C sp^2 bonds in the system. So, in practice, the whole spectrum is scaled such that we always have the same value for A_G. Both D and D′ bands present a similar nonmonotonic behavior, as reported in our previous study,[28] increasing with increasing ion dose (decreasing L_D) until L_D equals to roughly 4 nm then they start to decrease for smaller values of L_D. The intensities of the G and G′ bands always decrease with increasing ion dose. In the lower panel of Fig. 4, we show the areas of the D, D′, and G′ peaks, normalized by the area of the G peak. The solid lines are the results of the modeling described in Sec. V, to be discussed in more detail in that section.

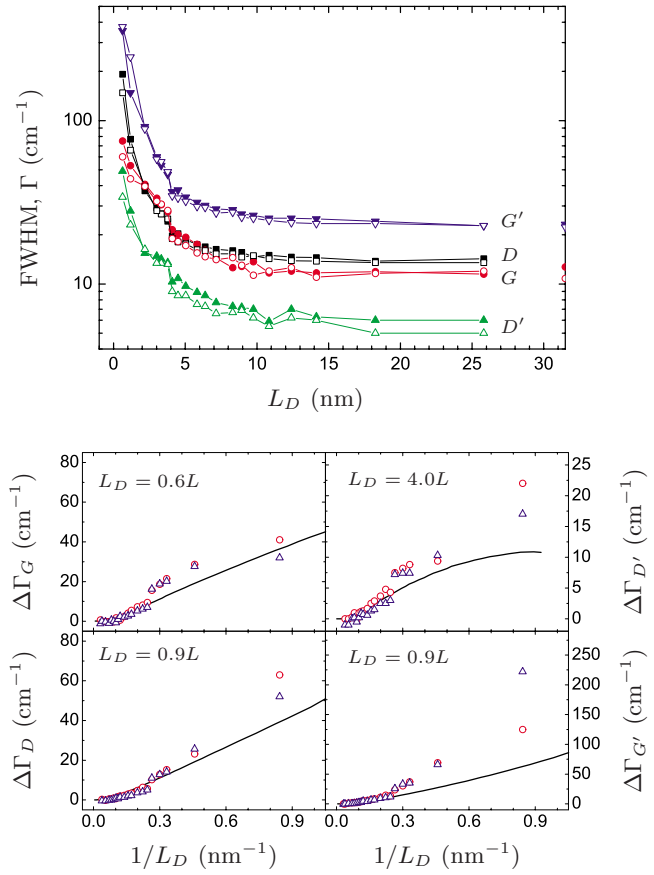

FIG. 3. (Color online) (Upper panel) FWHM of the D, G, D′, and G′ bands as function of the typical distance between defects (L_D) for the monolayer (S2). (Lower panel) Disorder contribution to the peak widths, $\Delta\Gamma$. Dots are experiments and solid lines are theoretical results based on the model described in Sec. IV.

D. Evolution of overtone and combination modes

In Fig. 5 we present the evolution of the G′ band and other second-order processes at graphene for four different ion doses. The G′ and 2D′ band intensities decrease as the width increase for increasing ion doses. The defect-related bands D+G at 2930 cm^{-1} and G+D′ at 2990 cm^{-1} can be observed at higher doses (10^{13} Ar$^+$/cm^2) but the 2D′ band is too weak to be seen in our measurement. At the dose of 10^{14} Ar$^+$/cm^2 we show a frequency downshift for all double-resonance features in agreement with the results of Sec. III A.

IV. MODELING DISORDER EFFECTS IN THE RAMAN LINEWIDTHS AND FREQUENCY SHIFTS: THE SPATIAL CORRELATION MODEL

As we saw in the previous section, disorder introduced by a random distribution of defects causes broadening, shifting, and increases the asymmetry of the Raman bands. In this section, we use the so-called "spatial-correlation model" to describe these effects in graphene. This model, which we briefly describe below, has been successfully applied to describe the evolution of the Raman spectra of disordered semiconductors.[32,33]

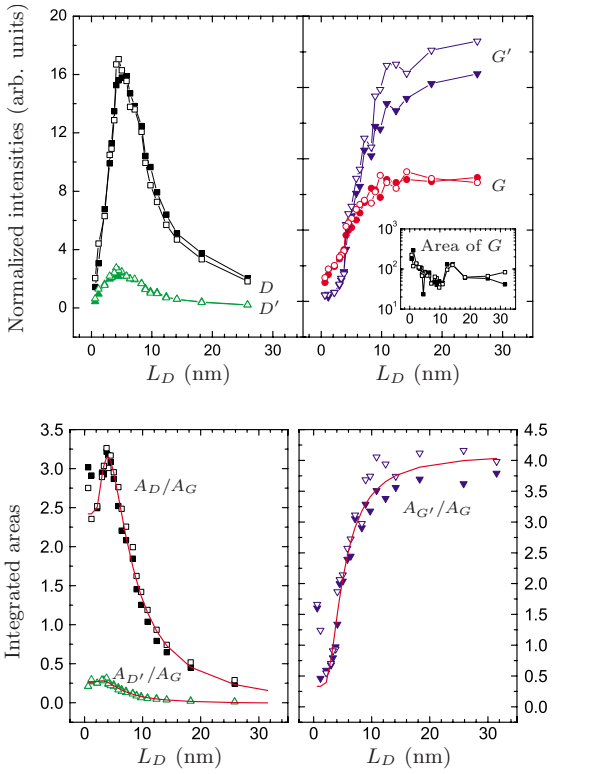

FIG. 4. (Color online) Normalized intensities (upper panel) and areas (lower panel) of D, D′, G, and G′ bands as function of L_D for the monolayer (S2). All quantities are normalized by the area of the G band (see the as-measured A_G in the inset to the upper-left panel). The solid lines in the lower panel are theoretical results based on the model described in Sec. V.

In a perfect system, the one-phonon Raman intensity $I_0(\omega)$ associated to vibrational mode of wave vector $\mathbf{q}_0$ and frequency $\omega(\mathbf{q}_0)$ is well described by a Lorentzian function,

$$I_0(\omega) \propto \frac{1}{[\omega - \omega(\mathbf{q}_0)]^2 + [\Gamma_0/2]^2}, \tag{1}$$

where the FWHM Γ_0 is the inverse phonon lifetime. For simplicity, we are considering a nondegenerate normal mode but this assumption can be easily generalized. In a perfect crystal, both electron-phonon and phonon-phonon (anharmonic effects) interactions contribute to the inverse lifetime. A disordered distribution of point defects will scatter phonons and it will also add a contribution to the FWHM by coupling phonons of wave vector $\mathbf{q}_0$ and $\mathbf{q}_0+\delta\mathbf{q}$. In the limit of low disorder, the coupling will be most effective for small δq, so the phonon wave packet in k space can be described by a Gaussian function $\exp[-(\mathbf{q}-\mathbf{q}_0)^2L^2/4]$ centered in $\mathbf{q}_0$ and having a width proportional to $1/L \approx \delta q$. Therefore, in real space L is a measure of the phonon coherence length,[34] which should also be a good measure of the average distance between point defects. Then, the Raman intensity for the disordered graphene $I(\omega)$ can be written as[32]

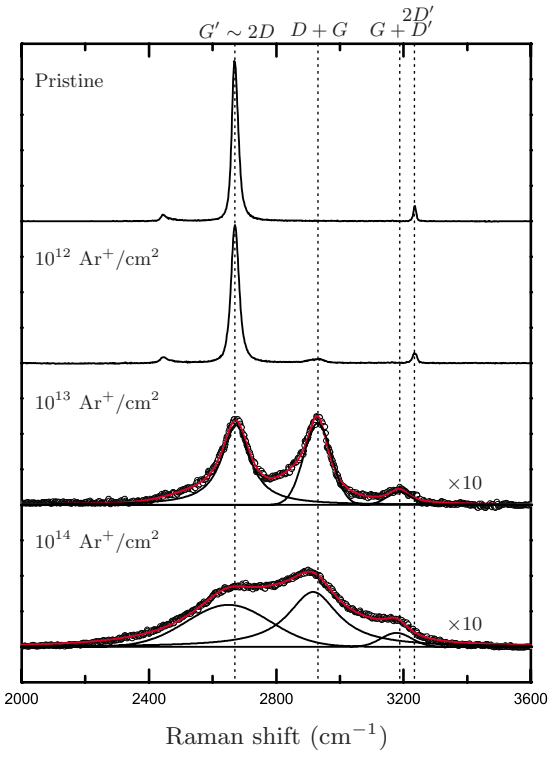

FIG. 5. (Color online) Evolution of G′ and other second-order peaks with increasing ion doses. The intensities of the two lower graphs are multiplied by a factor of 10 for sake of readability.

$$I(\omega) \propto \int_{BZ} d^2q \frac{W(\mathbf{q})\exp\left[\frac{-(\mathbf{q}-\mathbf{q}_0)^2L^2}{4}\right]}{[\omega-\omega(\mathbf{q})]^2+[\Gamma_0/2]^2}, \tag{2}$$

where the integral is taken over the two-dimensional Brillouin zone of graphene and $W(\mathbf{q})$ is a weighting function that describes wave-vector dependence of the electron-phonon coupling for the Raman process.

With this model we can calculate the full line shape of $I(\omega)$ and from that we can extract the disorder-induced peak shifts $\Delta\omega_{\mathbf{q}_0}$ (Fig. 2, lower panel) and the enhancement in FWHM $\Delta\Gamma_{\mathbf{q}_0}$ (Fig. 3, lower panel). We use experimentally available dispersion relations $\omega(\mathbf{q})$, so the only fitting elements in our model are (1) the relationship between the coherence length L and the typical interdefect distance L_D, and (2) the weighting function $W(\mathbf{q})$.

We now describe in more detail the application of the above model to the different Raman bands considered in this work.

(1) *G band.* The G band in perfect graphene is associated with phonons at the Γ point, i.e., $\mathbf{q}_0=0$. We consider that disorder mixes equally the Γ-point phonon with nearby phonons at both longitudinal optical (LO) and in-plane transverse optical (iTO) branches. We find that the best agreement with experiments is obtained by using a constant weighting function (which is equivalent to not use a weighting function at all). For the phonon dispersions, we take

$$\omega_{\mathrm{LO}}(q) = \omega_G + 181q - 230.29q^2,$$

$$\omega_{\mathrm{iTO}}(q) = \omega_G - 135.42q, \tag{3}$$

where $\omega_n(q)$ is in cm^{-1} (n=LO or iTO), ω_G=1580 cm^{-1} is our experimental G band frequency for pristine graphene, and q is measured from the Γ point in units of $\mathrm{Å}^{-1}$. These dispersions are taken from the work of Maultzsch *et al.*[35] by interpolating the frequencies at high-symmetry points and by averaging the dispersions between the Γ-K and Γ-M directions. Also, since the main contribution to the integral in Eq. (2) will come from near the Γ point, the Brillouin zone can be safely approximated by a circular disk and the integral will be in the radial coordinate only. With all these considerations, Eq. (2) becomes

$$I_G(\omega) \propto \sum_n \int 2\pi q dq \frac{\exp\left[\frac{-q^2L^2}{4}\right]}{[\omega-\omega_n(q)]^2+[\Gamma_0/2]^2}, \tag{4}$$

where the sum is over the two phonon branches.

(2) D′ *band.* The D′ band arises from intravalley phonons with a linear wave-vector dependence with respect to the laser energy. For our laser energy of 2.41 eV, we find $|\mathbf{q}_0|$ =0.42 $\mathrm{Å}^{-1}$ measured from the Γ point. Since the D′ band has been assigned to LO phonons,[18] only this branch is considered. We average over all possible directions θ of the wave vector $\mathbf{q}_0$ and, similarly to the case of the G band, there was no need to introduce the weighting function $W(\mathbf{q})$. Then, the D′ band intensity becomes

$$I_{D'}(\omega) \propto \int q dq d\theta \frac{\exp\left[\frac{-(\mathbf{q}-\mathbf{q}_0)^2L^2}{4}\right]}{[\omega-\omega_{\mathrm{LO}}(q)]^2+[\Gamma_0/2]^2}. \tag{5}$$

(3) *D band.* The D band arises from intervalley phonons which also show a linear wave-vector dependence with respect to the laser energy. In fact, for the laser energy of 2.41 eV, we also find $|\mathbf{q}_0|$=0.42 $\mathrm{Å}^{-1}$ for the D band but now $\mathbf{q}_0$ is measured from the K point. Since the D band has been assigned to iTO phonons along the K-M direction in the Brillouin zone,[36] we choose $\mathbf{q}_0$ along this direction and the weighting function $W(\mathbf{q})$ is also restricted to be nonzero only along the same direction. Mathematically, $W(\mathbf{q})=\delta(\theta-\theta_{\mathrm{KM}})f(q)$, where θ_{KM} indicates the K-M direction and $f(q)=1+a(q_0-q)$ is a function that linearizes the radial dependence of the electron-phonon coupling along the K-M direction near q_0. With these conditions, the D band intensity becomes

$$I_D(\omega) \propto \int dq \frac{f(q)\exp\left[\frac{-(q-q_0)^2L^2}{4}\right]}{[\omega-\omega_{\mathrm{iTO}}(q)]^2+[\Gamma_0/2]^2}. \tag{6}$$

For the iTO phonon dispersion along K-M, we use the phonon dispersion as measured by Grüneis *et al.*[37]

$$\omega_{\mathrm{iTO}}(q) = \omega_K + 589.35q - 485.46q^2, \tag{7}$$

where ω_{iTO} is in cm^{-1} and q is measured from the K point in $\mathrm{Å}^{-1}$.

(4) G′ *band.* The G′ band is related to a double-resonance process associated to the same intervalley phonons as the D

band. For this reason, the expression for the intensity becomes more complicated and it involves a double integral in the forward (q) and backward (q') phonon wave vectors. Using the same considerations for the electron-phonon matrix elements, which essentially select phonons in the K-M direction, we have

$$I_{G'}(\omega) \propto \int dq dq' \frac{f(q)f(q')\exp\left[\frac{-[(q-q_0)^2+(q'-q_0)^2]L^2}{4}\right]}{[\omega-\omega_{\mathrm{iTO}}(q)-\omega_{\mathrm{iTO}}(q')]^2+[\Gamma_0/2]^2}, \tag{8}$$

where $f(q)$ is the same linear function as in the D band case and q_0 is also the same. We also impose that the same relation between L and L_D must be valid for the D and G′ bands.

In the lower panels of Figs. 2 and 3, we see the results for the data fitting of the frequency shifts and widths, respectively, as described above. Notice that the general agreement is very good, specially for large values of L_D. Indeed, this spatial-correlation model, for its perturbative character, is not expected to be valid in the highly disordered regime. In the figures, we also show the best relationships between L and L_D in each case (obtained by the fits). It is nice to see that L and L_D are similar to each other. Again, we stress that this was not imposed but it comes automatically from the fitting procedure. That means that the disordered-induced phonon coherence length is of the same order of the typical interdefect distance, which is quite reasonable. We also emphasize that there is no reason to expect that the same relation between L and L_D should be found for the different phonon modes since different modes should have different defect scattering cross sections. From our results, it seems that the D′ modes are the most affected by disorder, showing a smaller coherence length than the other modes for the same amount of disorder. Finally, the model allows us to explain the greater increase in FWHM of the modes near K with respect to the modes near Γ as simply a consequence of the larger magnitude of phonon dispersions near K.

V. MODELING DISORDER EFFECTS IN THE RAMAN INTENSITIES: THE "LOCAL ACTIVATION" MODEL

The phenomenological model described in the previous section allows one to investigate the disorder effects on the Raman linewidths and frequency shifts. However, this model is not appropriate to describe the relative intensities (or integrated areas) of the different Raman bands since it misses one important physical ingredient: the disorder-induced D and D′ bands are "locally activated," that is, these modes become Raman active only in the near vicinity of a point defect. Recently, we proposed a model to describe these effects in graphene samples with a random distribution of point defects,[28] which we call here "local activation model." In that work, the dependence of the intensity ratio I_D/I_G on L_D was found to follow very accurately an analytical formula. In this present work, we choose to use the same expression to fit the ratio between integrated areas A_D/A_G and $A_{D'}/A_G$, shown in the lower panel of Fig. 4, rather than the ratio between intensities. Then

$$\frac{A_X}{A_G}(L_D) = C_A \frac{r_A^2 - r_S^2}{r_A^2 - 2r_S^2}\left[e^{-(\pi r_S^2/L_D^2)} - e^{-[\pi(r_A^2-r_S^2)/L_D^2]}\right] + C_S\left[1 - e^{-(\pi r_S^2/L_D^2)}\right], \tag{9}$$

where X denotes either D or D′, and r_S and r_A are two characteristic length scales associated with the presence of defects in the system. The first is interpreted as the radius of a structural damaged region measured from the point of impact of the ions and the second is a defect-activated region where no damage in the structure is observed but where there is a mixing of Bloch states near the K and K′ points caused by the defect. This formula is obtained by taking into account two competing mechanisms for the increase and decrease in the defect-activated bands. First, these bands increase with increasing disorder because they become Raman active in the near vicinity of a point defect, at a distance $r_A - r_S$ from it. This distance is a rough measure of the length traveled over the lifetime of the electron-hole pair, v_F/ω_X, where v_F is the graphene Fermi velocity.[38] Second, the same bands decreases with increasing disorder by the progressive disorganization of the hexagonal network of carbon atoms, which occurs within at a length scale r_S from the Ar^+ ions impact points. By solving rate equations for the combination of these two processes, we arrive at Eq. (9).[28] The lower left panel of Fig. 4 shows that this analytical expression fits nearly perfectly the quantities A_D/A_G and $A_{D'}/A_G$. For the D band, the fitting parameters are r_S=2.6 nm, r_A=4.1 nm, C_S=2.4, and C_A =3.6, whereas for the D′ band we have r_S=2.6 nm, r_A =3.8 nm, C_S=0.28, and C_A=0.19. Notice that we obtain the same value of r_S for the two modes, indicating the indeed r_S is a geometrical, structure-related length. Also, we find 1.5 and 1.3 nm for the spatial extent of the Raman processes $r_A - r_S$, in the same order of magnitude as the rough estimates v_F/ω_D=4.3 nm and $v_F/\omega_{D'}$=3.6 nm. More interestingly, the ratio between $r_A - r_S$ for the D and D′ bands matches very closely the ratio of inverse frequencies $\omega_{D'}/\omega_D \approx 1.2$.

Similar ideas can be applied for the $A_{G'}/A_G$ ratio, but in this case, since the G′ band is already active for pristine graphene, the intensity ratio is only affected by the disorganization of the hexagonal network, leading to a ratio decrease as a function of increasing disorder described by the simple formula

$$\frac{A_{G'}}{A_G}(L_D) = \frac{A_{G'}}{A_G}(\infty) - B\left[1 - e^{-\pi r_S^2/L_D^2}\right], \tag{10}$$

where $A_{G'}/A_G(\infty)$ is the area ratio for pristine graphene. The fitting of the experimental data, shown in the lower right panel of Fig. 4 gives in this case r_S=2.5 nm, also similar to the structural damage length obtained for the D and D′ bands. This result is in accordance with the typical defect-size estimates found from STM analysis. Figure 6 shows the compilation of the results obtained from this analysis. We note that the distribution of the defect size is very sparse but

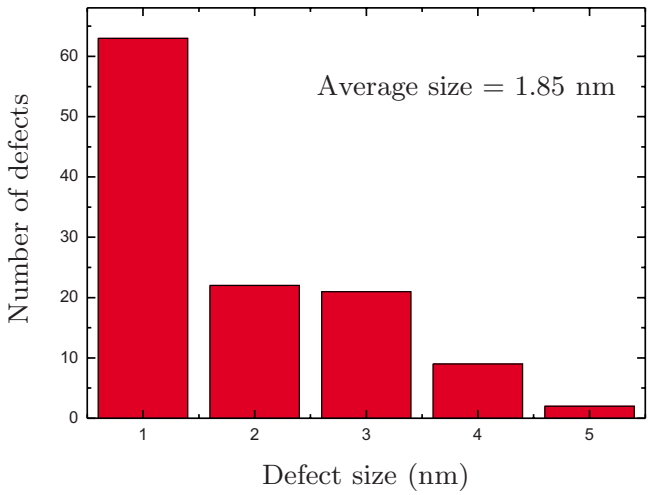

FIG. 6. (Color online) Distribution of defect size measured by STM image analysis of a HOPG bombarded surface.

the average size is 1.85 nm, in the same magnitude of the fitting result for r_S.

VI. RAMAN SPECTRA OF DISORDER MULTILAYER GRAPHENE

For completeness, we now analyze how the Raman features change for graphenes with different number of layers as sample S1 is subjected to increasing ion bombardment. This analysis will be qualitative, mostly due to the presence of many peaks in the double-resonance bands, which makes quantitative analysis more ambiguous.

A. Frequency

Figure 7 shows the evolution of the frequencies of the Raman peaks (D, G, and G′) with L_D for M, B, T, and 50 ~layers (HOPG) graphene samples. We observed that the frequencies do not change considerably with decreasing L_D. While the G and D′ bands have just one peak for any number of layers, the G′ and D bands are constituted, respectively, by one, four, six, and two peaks for monolayer, bilayer, trilayer, and many layers of graphene. Up to the 10^{13} Ar^+/cm^2 dose the frequency changes a little for few layers while for HOPG no change was observed. The result in HOPG happens because the micro-Raman spectroscopy collects data from the inner layers and the bombardment affects mainly the surface.

In Fig. 8 we plot the fitted peaks of the D band and G′ band with the frequency divided by 2 for every number of layers at a given ion dose of 10^{12} Ar^+/cm^2. Both bands have similar line shape for each sample but the G′/2 peaks are always shifted 4.5 cm^{-1} to lower frequency with respect to the D peaks, independent on the number of layers. Therefore, this behavior, which is related with the double-resonance feature of the Raman scattering in graphitic materials, is independent on the number of layers.

B. Width

As stated in the previous section, for any multilayer graphene (including graphite), the D and G′ bands are composed of more than one peak and, therefore, instead of the analysis of each peak width individually or the width of the whole band, we plot the integrated area, A_X, divided by the intensity, I_X, for X=D, G, D′, and G′ bands, for every number of layers (see Fig. 9). For a single peak this corresponds exactly to the evolution of the width of the band. It is more intuitive to compare this quantity since the area represents all possible Raman scattering occurring for a given process. What we note here is that, in all cases, this A_X/I_X increases with the bombardment, which is consistent with what has been discussed for the FWHM monolayer (see Sec. III B). While for few layer graphenes this increase is remarkable, the effects decrease with the number of layers, and for graphite the change is much less pronounced. This is another confirmation that our bombardment with low-energy (90 eV) ions affects mostly the upper layers.

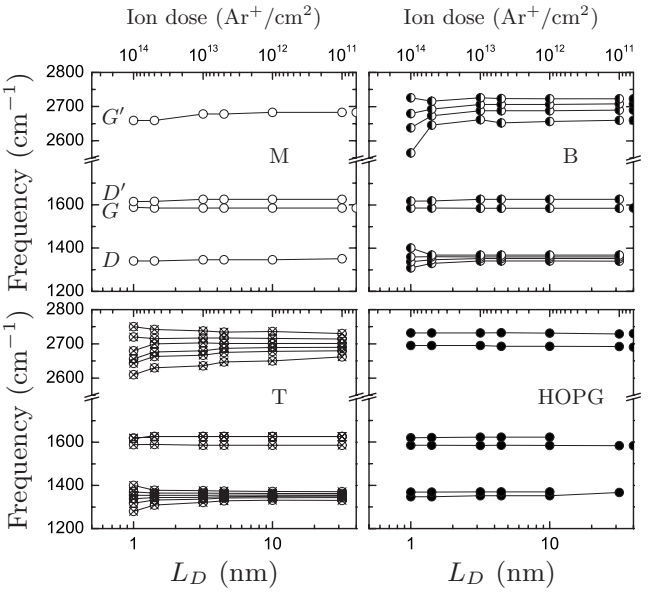

FIG. 7. Frequency of the D, G, D′, and G′ peaks for different number of graphene layers as a function of L_D (lower axis) or equivalently the ion dose (upper axis).

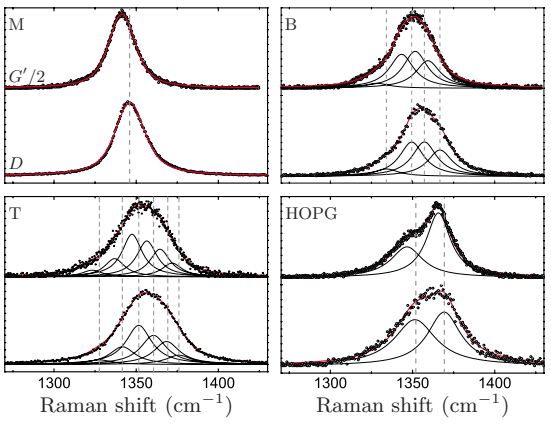

FIG. 8. (Color online) Comparison between the D bands and G′ bands with the frequency divided by 2 of M, B, and T graphenes and graphites (HOPG) at a given ion dose of 10^{12} Ar^+/cm^2.

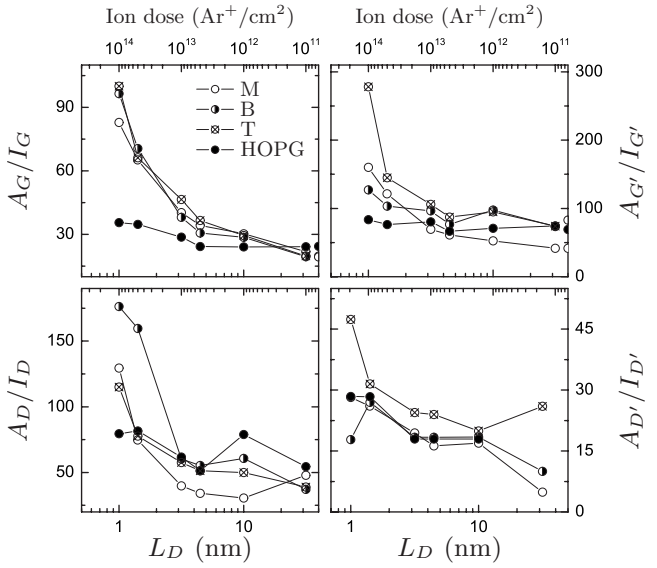

FIG. 9. Integrated area divided by the intensity of the D, G, D′, and G′ bands for monolayer, bilayer, and trilayer graphenes and graphites.

VII. CONCLUSION

We have here presented a thorough analysis of the Raman spectra for monolayer, bilayer, trilayer, and many layers graphene samples as they are submitted to the bombardment of low-energy (90 eV) Ar^+ ions. The effect of such ions on the graphene is to change its structure, which immediately reflects on the Raman spectra. We show specially how the frequency, width, intensity, and integrated area for the D, G, D′, and G′ bands evolve with increasing disorder. The disorder evolution for all these Raman band parameters has been modeled. The evolution of frequency and width are explained by a spacial correlation model while the intensity and integrated area are explained by the local activated model. Other details such as the behavior of overtone and combination modes, the difference between first- and second-order features, and the evolution with the number of layers are also addressed.

ACKNOWLEDGMENTS

The authors thank C. Vilani for the AFM image and G. N. Fontes for helping with the ion bombardment procedure. A.J. acknowledges support from AFOSR/SOARD (Award No. FA9550-08-1-0236). This work was financed by the Brazilian National Institute of Metrology, Standardization and Industrial Quality (Inmetro) and by the Brazilian Science foundations CNPq, FAPERJ, CAPES, INCT – Nanomateriais de Carbono and FINEP.

[1] P. R. Wallace, Phys. Rev. **71**, 622 (1947).
[2] K. S. Novoselov, A. K. Geim, S. V. Morozov, D. Jiang, Y. Zhang, S. V. Dubonos, and I. V. G. A. A. Firsov, Science **306**, 666 (2004).
[3] Y. Zhang, Y.-W. Tan, H. L. Stormer, and P. Kim, Nature (London) **438**, 201 (2005).
[4] A. K. Geim and K. S. Novoselov, Nature Mater. **6**, 183 (2007).
[5] S. V. Morozov, K. S. Novoselov, M. I. Katsnelson, F. Schedin, D. C. Elias, J. A. Jaszczak, and A. K. Geim, Phys. Rev. Lett. **100**, 016602 (2008).
[6] A. A. Balandin, S. Ghosh, W. Bao, I. Calizo, D. Teweldebrhan, F. Miao, and N. Chun, Nano Lett. **8**, 902 (2008).
[7] X. Liang, Z. Fu, and S. Y. Chou, Nano Lett. **7**, 3840 (2007).
[8] Y. Zhang, J. P. Small, W. V. Pontius, and P. Kim, Appl. Phys. Lett. **86**, 073104 (2005).
[9] C. Berger *et al.*, J. Phys. Chem. B **108**, 19912 (2004).
[10] S. Bunch, Y. Yaish, M. Brink, K. Bolotin, and P. L. McEuen, Nano Lett. **5**, 287 (2005).
[11] I. L. Aleiner and K. B. Efetov, Phys. Rev. Lett. **97**, 236801 (2006).
[12] A. Altland, Phys. Rev. Lett. **97**, 236802 (2006).
[13] V. M. Pereira, J. M. B. Lopes dos Santos, and A. H. Castro Neto, Phys. Rev. B **77**, 115109 (2008).
[14] M. S. Dresselhaus and R. Kalish, *Ion Implantation in Diamond, Graphite and Related Materials*, Springer Series in Materials Science Vol. 22 (Springer-Verlag, Berlin, 1992).
[15] Philos. Trans. R. Soc. London, Ser. A **362** 1824 (2004), special issue on Raman Spectroscopy in Carbons: From Nanotubes to Diamond, compiled by A. C. Ferrari and J. Robertson.
[16] F. Tuinstra and J. L. Koenig, J. Chem. Phys. **53**, 1126 (1970).
[17] C. Thomsen and S. Reich, Phys. Rev. Lett. **85**, 5214 (2000).
[18] R. Saito, A. Jorio, A. J. A. G. Souza Filho, G. G. Dresselhaus, M. S. Dresselhaus, and M. Pimenta, Phys. Rev. Lett. **88**, 027401 (2001).
[19] M. A. Pimenta, G. Dresselhaus, M. S. Dresselhaus, L. G. Cançado, A. Jorio, and R. Saito, Phys. Chem. Chem. Phys. **9**, 1276 (2007).
[20] A. Jorio, M. S. Dresselhaus, and G. Dresselhaus, *Carbon Nanotubes: Advanced Topics in the Synthesis, Structure, Properties and Applications*, Springer Series in Topics in Applied Physics Vol. 111 (Springer-Verlag, Berlin, 2008).
[21] I. O. Maciel *et al.*, Nature Mater. **7**, 878 (2008).
[22] V. Perebeinos, J. Tersoff, and P. Avouris, Phys. Rev. Lett. **94**, 027402 (2005).
[23] N. Bonini, M. Lazzeri, N. Marzari, and F. Mauri, Phys. Rev. Lett. **99**, 176802 (2007).
[24] G. M. Rutter, J. N. Crain, N. P. Guisinger, T. Li, P. N. First, and J. A. Stroscio, Science **317**, 219 (2007).
[25] L. G. Cançado, A. Jorio, and M. A. Pimenta, Phys. Rev. B **76**, 064304 (2007).
[26] A. C. Ferrari *et al.*, Phys. Rev. Lett. **97**, 187401 (2006).
[27] A. Jorio, M. M. Lucchese, F. Stavale, and C. A. Achete, Phys. Status Solidi B **246**, 2689 (2009).
[28] M. M. Lucchese, F. Stavale, E. H. M. Ferreira, C. Vilani, M. V. O. Moutinho, R. B. Capaz, C. Achete, and A. Jorio, Carbon **48**, 1592 (2010).
[29] A. Gupta, G. Chen, P. Joshi, S. Tadigadapa, and P. C. Eklund, Nano Lett. **6**, 2667 (2006).

[30] L. M. Malard, M. H. D. Guimarães, D. L. Mafra, M. S. C. Mazzoni, and A. Jorio, Phys. Rev. B **79**, 125426 (2009).
[31] L. G. Cançado, M. A. Pimenta, R. Saito, A. Jorio, L. O. Ladeira, A. Grueneis, A. G. Souza-Filho, G. Dresselhaus, and M. S. Dresselhaus, Phys. Rev. B **66**, 035415 (2002).
[32] K. K. Tiong, O. M. Amirtharaj, F. H. Pollak, and D. E. Aspnes, Appl. Phys. Lett. **44**, 122 (1984).
[33] H. Richter, Z. P. Wang, and L. Ley, Solid State Commun. **39**, 625 (1981).
[34] R. Shuker and R. W. Gammon, Phys. Rev. Lett. **25**, 222 (1970).
[35] J. Maultzsch, S. Reich, C. Thomsen, H. Requardt, and P. Ordejón, Phys. Rev. Lett. **92**, 075501 (2004).
[36] D. L. Mafra, G. Samsonidze, L. M. Malard, D. C. Elias, J. C. Brant, F. Plentz, E. S. Alves, and M. A. Pimenta, Phys. Rev. B **76**, 233407 (2007).
[37] A. Grüneis *et al.*, Phys. Rev. B **80**, 085423 (2009).
[38] C. Casiraghi, A. Hartschuh, H. Qian, S. Piscanec, C. Georgi, A. Fasoli, K. S. Novoselov, D. M. Basko, and A. C. Ferrari, Nano Lett. **9**, 1433 (2009).